International Journal of Greenhouse Gas Control 112 (2021) 103476

Contents lists available at ScienceDirect

International Journal of Greenhouse Gas Control

journal homepage: www.elsevier.com/locate/ijggc

Detection and quantification of a release of carbon dioxide gas at the seafloor using pH eddy covariance and measurements of plume advection

Dirk Koopmans [a,*], Volker Meyer [a], Allison Schaap [b], Marius Dewar [c], Paul Färber [a], Matthew Long [d], Jonas Gros [e], Douglas Connelly [b], Moritz Holtappels [f]

[a] Max Planck Institute for Marine Microbiology, Celsiusstr. 1, D-28359 Bremen, Germany
[b] National Oceanography Centre, European Way, Southampton, SO14 3ZH, UK
[c] Plymouth Marine Laboratory, Prospect Place, Plymouth, PL1 3DH, UK
[d] Woods Hole Oceanographic Institution, Marine Chemistry and Geochemistry Department, Woods Hole, Massachusetts 02543, USA
[e] GEOMAR Helmholtz Centre for Ocean Research Kiel, Wischhofstr. 1-3, D-24148 Kiel, Germany
[f] Alfred Wegener Institute for Marine and Polar Research, Am Handelshafen 12, D-27570 Bremerhaven, Germany

ARTICLE INFO

Keywords:
CO_2 vent
Offshore CCS
Leakage detection and quantification
Marine sediment
Proton flux

ABSTRACT

We detected a controlled release of CO_2 (g) with pH eddy covariance. We quantified CO_2 emission using measurements of water velocity and pH in the plume of aqueous CO_2 generated by the bubble streams, and using model predictions of vertical CO_2 dissolution and its dispersion downstream. CO_2 (g) was injected 3 m below the floor of the North Sea at rates of 5.7–143 kg d^{-1}. Instruments were 2.6 m from the center of the bubble streams. In the absence of injected CO_2, pH eddy covariance quantified the proton flux due to naturally-occurring benthic organic matter mineralization (equivalent to a dissolved inorganic carbon flux of 7.6 ± 3.3 mmol m^{-2} d^{-1}, s.e., $n = 33$). At the lowest injection rate, the proton flux due to CO_2 dissolution was 20-fold greater than this. To accurately quantify emission, the kinetics of the carbonate system had to be accounted for. At the peak injection rate, 73 ± 13% (s.d.) of the injected CO_2 was emitted, but when kinetics were neglected, the calculated CO_2 emission was one-fifth of this. Our results demonstrate that geochemical techniques can detect and quantify very small seafloor sources of CO_2 and attribute them to natural or abiotic origins.

1. Introduction

To achieve net carbon neutrality by 2050, as many governments have pledged, technology will be needed to offset CO_2 emissions during a transition to greener energy and industrial production. Carbon capture and storage (CCS) can help meet this need (IPCC, 2019). In 2019, 25 Mt of CO_2 were stored in terrestrial and offshore reservoirs (GCCSI, 2019). This is an increase over prior years but remains small compared to global CO_2 emissions of 42 Gt that year. The primary obstacles that CCS must overcome for more widespread use are insufficient public support and cost. It can be argued that public support is more important. Government subsidies for low-carbon energy such as offshore wind are similar to the subsidies that would be needed for a private CCS industry to develop (Bui et al., 2018). Highlighting the importance of public support, a terrestrial CCS project in the Netherlands was canceled due to public concern for potential environmental consequences of CO_2 leakage, among other factors (Feenstra et al., 2010). To address public concern, offshore CCS may be preferred over terrestrial CCS. In offshore CCS, CO_2 would be injected into saline aquifers or depleted oil and natural gas reservoirs hundreds to thousands of meters below the seafloor. Offshore carbon storage capacity is sufficient for mitigating emissions (e.g., Vangkilde-Pedersen et al., 2009), and offshore CCS has successfully been demonstrated at Sleipner and Snøhvit, Norway, and Tomakomai, Japan (Furre et al., 2017; Sawada et al., 2018). Nevertheless, there is public concern for the resilience of marine ecosystems to environmental damage that could be caused by offshore CCS operations (Schumann et al., 2014). Effective offshore monitoring technology can highlight issues and allow the development of strategies to mitigate risk.

Our research was conducted as part of a larger study with the aim of examining the effectiveness of chemical, acoustic, and optical sensors at detecting and quantifying a controlled release of CO_2 at the seafloor at very small rates (5.7 to 143 kg d^{-1}). For context on the magnitude of these rates, the Peterhead CCS project was designed to inject 1 million tons of CO_2 per year into the depleted Goldeneye hydrocarbon gas field

* Corresponding author.
E-mail address: dirk.koopmans@gmail.com (D. Koopmans).

https://doi.org/10.1016/j.ijggc.2021.103476
Received 24 December 2020; Received in revised form 8 August 2021; Accepted 27 September 2021

at the experimental release site (Dean and Tucker, 2017). If 0.01% of this CO_2 leaked back to the atmosphere, the emission would be 270 kg d^{-1}. This is the rate of CO_2 emission by a fuel-efficient car (producing 120 g CO_2 km^{-1}) travelling at ~100 km h^{-1}. The goal of quantifying smaller leaks than this is to demonstrate a technical competence that can be used to ensure the integrity of storage. The rates of release are physically realistic: they are in the range of leakages that can occur along the outside of wells due to the fracturing of sediments caused while drilling (Vielstädte et al., 2019). Fortunately, the adverse environmental consequences of leaks at this low rate are minimal, with a footprint of potential harmful effects ($\Delta pH > 0.1$ unit) on the order of a hundred square meters or less (Blackford et al., 2020; Vielstädte et al., 2019). The adverse environmental consequences are also transient, with recovery occurring within a few weeks (Blackford et al., 2014). Therefore, if these leaks can be detected, then leakage into overlying water can be detected at a lower rate of emission than that which causes significant adverse environmental consequences.

A substantial challenge for the identification of a small leak is the risk of false positives, i.e., anomalously high environmental CO_2 concentrations that are attributed to CCS, but are nevertheless caused by naturally-occurring organic matter mineralization. False positives have brought accusations of leakage against a terrestrial CCS site (Beaubien et al., 2013; Romanak et al., 2013) and a temporary project suspension for offshore CCS (CSLF, 2017). Both of these events eroded public trust. Offshore CCS monitoring will face an enhanced risk of false positives due to the incentive to identify small leaks, which requires the ability to confidently differentiate a small signal from a time-varying background. Therefore, detection of CO_2 emission is only one of the tasks that will be required for monitoring. A robust CCS seafloor monitoring program would include phases of detection, attribution, quantification, and environmental assessment (Blackford et al., 2015). This program would be based on complementary technologies. To detect small leaks of CO_2 at the seafloor, active acoustics (i.e., multibeam sonar) would likely be used. Sonar detected a 29 kg d^{-1} experimental CO_2 release at 110 m depth in a prior study (Dean et al., 2020) and is used for monitoring the seafloor at the Sleipner site (Linke et al., 2014). However, acoustic techniques have limitations. CO_2 bubbles, methane bubbles, and the swim bladders of fish all generate similar acoustic returns. In addition, gas concentration within bubbles cannot be resolved (e.g., Long et al., 2020), and backscatter does not correspond to bubble size, complicating quantification of emission. Therefore, acoustic techniques would likely be aided by other, complementary techniques, including optical sensors (Delwiche and Hemond, 2017a, 2017b), passive acoustics (Leighton and White, 2012), and geochemical leak detection (Blackford et al., 2015). pH eddy covariance is capable of quantifying naturally-occurring benthic biological CO_2 production (Long et al., 2015). Therefore, we expect it to be highly sensitive to benthic CO_2 emission. Turbulence is the dominant mechanism responsible for the vertical exchange of mass (such as CO_2) with overlying air or water in terrestrial and aquatic environments. Eddy covariance quantifies the vertical flux of a solute from the covariance of high frequency (e.g., > 1 Hz), turbulent fluctuations in vertical velocity and solute concentration (Berg et al., 2003). pH and O_2 concentrations can be determined at a high-enough frequency for the technique. The dissolution of CO_2 (g) in seawater produces hydrogen ions according to Zeebe and Wolf-Gladrow (2001) as follows

$$CO_2(aq) + H_2O \rightleftharpoons H_2CO_3 \rightleftharpoons HCO_3^- + H^+ \rightleftharpoons CO_3^{2-} + 2H^+ \quad (1)$$

Because $pH = -\log_{10}[H^+]$, pH eddy covariance would detect a source of CO_2 at the seafloor.

The primary goal of this study was to detect a source of CO_2 at the seafloor during a controlled, experimental release of CO_2 (g). A second goal was to quantify CO_2 released to the water column. To detect a CO_2 source (i.e., a bubble stream), we developed a pH eddy covariance system to quantify the vertical pH flux through the benthic boundary layer (the lowermost portion of the water column where current velocity is affected by bed friction). However, because CO_2 emission from the seafloor was a point source, and not spatially uniform during the experiment, eddy covariance measurements did not quantify the total CO_2 emitted. Instead, we quantified CO_2 emitted from the seafloor by calculating the advection of enriched dissolved inorganic carbon (DIC) in the plume of aqueous CO_2 generated by bubble dissolution. The mass transport of enriched DIC in the plume was calculated from current velocity, direction, and pH measured by eddy covariance instruments. Supporting measurements of high-accuracy pH and alkalinity were made by lab-on-chip sensors. The vertical distribution of DIC in the plume and its dispersion downstream were predicted by complementary numerical models. The result was adjusted to fit the observed pH at two heights above the seafloor determined by a lab-on-chip pH sensor.

2. Materials and methods

2.1. Study site and the experimental release of CO_2

To provide an opportunity to demonstrate a technical competence at ensuring the integrity of offshore CO_2 storage, a controlled release of 675 kg of CO_2 (g) was conducted in the North Sea. The injection site (57° 59.574′ N, 0° 22.460′ W) was a candidate CCS site, a depleted hydrocarbon gas reservoir located 140 km northeast of Aberdeen, Scotland. The experiment was conducted in May of 2019 with support from two research vessels, the RRS James Cook (cruise 180) and the R/V Poseidon (cruise 534). Details of the site and the experimental design are presented in Flohr et al. (2021b). For the injection, a curved, 9-m pipe was inserted into surficial sediments to position a diffuser tip 3 m beneath the sediment surface at a distance of 7 m from the pipe inlet, which remained above the sediment surface. A remotely operated vehicle (ROV) connected the pipe inlet to CO_2 (g) delivered from a pressurized container at the seafloor. To minimize hydrodynamic interference, the CO_2 (g) container was positioned 80 m off-axis from the predominant (north-south) flow direction. CO_2 monitoring equipment including the eddy covariance instrument frame were positioned at the release site by the ROV.

The sediments overlying the pipe were sandy muds, with layers of muddy sands with a porosity of 50%. Sediments were predominantly quartz with minor calcite and clay mineral fractions (Lichtschlag et al., 2021). CO_2 was injected through the pipe continuously from 11 May to 22 May 2019. The rate of gas injection was increased step-wise, with rates of 5.7, 14.3, 28.5, 85.5, and 143 kg CO_2 d^{-1}. Eddy covariance instruments were positioned 4 m to the south of the buried diffuser tip, the expected initial point of emission. Other monitoring instruments were positioned primarily to the east and west of the point of release to minimize hydrodynamic interference.

2.2. Eddy covariance measurements

Eddy covariance flux was calculated according to Berg et al. (2003) as

$$\overline{)flux} = \overline{u_z' c'} \quad (2)$$

where u_z is the vertical water velocity, c is solute concentration, the prime symbol indicates a fluctuating component from which the mean has been subtracted, and the overbar indicates averaging. Water velocities were determined at 16 Hz in three dimensions with an acoustic Doppler velocimeter (ADV; Nortek Vector, Nortek AS). pH and dissolved oxygen were determined at the measurement volume of the ADV which was positioned 16 cm above the seafloor. Dissolved oxygen was measured using a non-stirring sensitive mini-optode (Holtappels et al., 2015) with a $t_{90} < 0.4$ s (OXR-430-UHS, Pyroscience, GmbH). For LED-excitation of the sensor, and quantification of the resulting fluorescence, an oxygen meter (FSO2; Pyroscience, GmbH) was placed in a submersible housing with an optical port. Analog output from the meter

was recorded on an analog input channel of the ADV. We chose 16 cm as the measurement height because we expected the greatest DIC enrichment just above the seafloor. Additionally, for eddy covariance measurements, selection of the measurement height is a trade-off between signal intensity and signal frequency (Long, 2021). Close to the seafloor upwards-moving eddies have dispersed less. This makes differences in their solute concentrations from the overlying water column stronger.

The eddy covariance pH signal was determined by an Ion Sensitive Field Effect Transistor (ISFET; Microsens SA). Its operation relied on custom-made components following the principles of Long et al. (2015). To exclude the effect of light-sensitivity during calibrations and field work, a narrow opaque cylinder was designed to house the ISFET. Water was pumped into the cylinder and across the face of the sensor (Fig. 1). A sampling tube, 7 cm long and 2 mm in inner diameter, was used to draw water from the measurement volume of the ADV. ISFET function requires a reference voltage, for this we used a reference electrode with minimal stirring sensitivity based on a ceramic membrane design. The reference was integrated into the sensor flow-path (Fig 1). The signal of the ISFET was amplified ten-fold using an auto-zeroing galvanic isolation amplifier that has been previously used for eddy covariance O_2 measurement (Berg et al., 2003). For pH measurement, the amplifier was modified with a custom input stage for source-drain operation of the

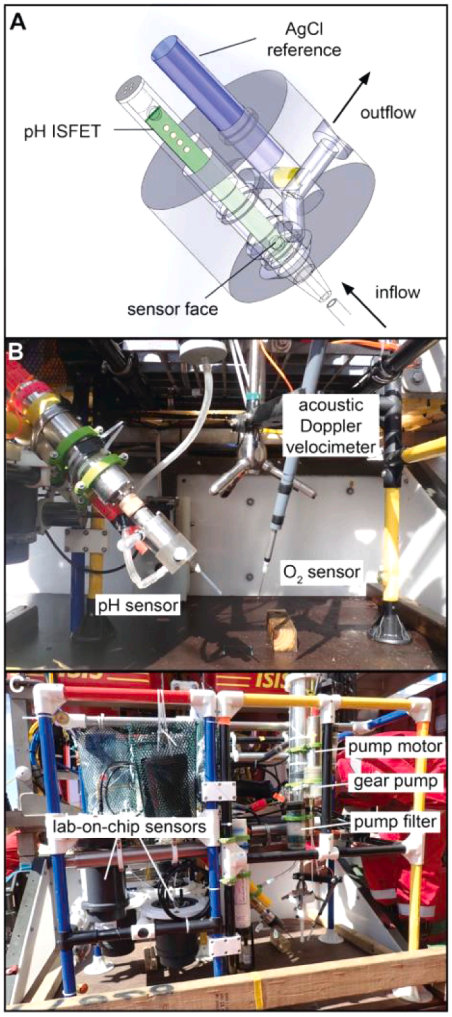

Fig. 1. Design and deployment of the pH eddy covariance system. A) Illustration of the pH ISFET housing, integrated AgCl reference, and its ceramic membrane (yellow) in the path of pumped flow. B) Arrangement of the intake of the pH sensor and the tip of the O_2 sensor outside the measurement volume of the acoustic Doppler velocimeter. C) Eddy covariance hardware and lab-on-chip sensors mounted to a fiberglass frame for deployment.

ISFET. The voltage response of the amplified ISFET signal to a change in pH was close to 590 mV per unit of pH. The precision of the amplified signal was smaller than 0.002 pH units. The amplifier was modified to compensate for the effect of temperature on the reported pH signal (25 to 40 mV per °C). To make this compensation, a temperature sensor (negative temperature coefficient thermistor) was mounted at the ISFET sensor face. Temperature measurements were used to compensate low frequency contributions (< 0.01 Hz) to the ISFET signal. To reduce noise generated by the isolation amplifier, a signal conditioning board was added to the ADV. This board also expanded the analog input range of the ADV to +/- 5 V. To ensure that the sensor signal would remain in this range, the amplifier auto-zeroed the signal every half hour. Once per deployment we made a single-point calibration of the ISFET signal to background pH (8.04) determined in situ by a pH lab-on-chip sensor (accuracy +/- 0.003 units, precision 0.001 units; National Oceanography Centre, Southampton, UK). The lab-on-chip sensor was positioned on the same frame as the eddy covariance instruments (Fig 1), and measured pH at the same height as the ISFET (16 cm).

A reversible gear pump was developed to draw water from the measurement volume of the ADV past the ISFET. The pump gears were mounted in a 3D printed housing and operated by a motor that was programmed to reverse direction for one minute out of every thirty. The reversals cleared the pump tubing of accumulated debris. The pumped flow rate was 150 ml min^{-1}. Continuous flow of water past the ceramic membrane of the reference sensor effectively eliminated its residual sensitivity to changes in water velocity (stirring sensitivity). The 90% response time of the ISFET (mean of the responses to pH increase and decrease) was 1.2 s. This is slower than the response time typically targeted with eddy covariance sensors, but it is rapid enough to record almost all of the turbulent frequencies that typically contribute to eddy covariance fluxes (e.g., 1 Hz to 0.001 Hz; Berg et al., 2013). We examined the fraction of the flux signal that was lost due to the relatively slow speed of this sensor by examining the frequencies at which contributions to the measured flux occurred during the experiment. We found that turbulent contributions to oxygen flux began at 1 Hz and turbulent contributions to pH flux began at 0.5 Hz (data not shown). In oxygen fluxes, the contribution of frequencies between 1 Hz and 0.5 Hz was less than 10% of the total signal. Therefore, pH flux underestimation due to the slower response time of this sensor was also likely to have been less than 10%. We found that during the first 48 h of eddy covariance measurements at the site, the pH signal recorded by two identical ISFET sensors was too noisy for accurate flux calculations (data not shown). The noise was unrelated to ROV operations. Bresnahan et al., (2014) identify causes of transient instability and inaccuracy that occur with the first use of a pH ISFET that likely contributed to the noise that we observed. They recommend pre-conditioning the sensor in seawater to alleviate many of these issues.

The eddy covariance pH and O_2 sensors were mounted at the measurement volume of an ADV on a lightweight fiberglass frame. An eddy covariance sensor that is placed too close to the ADV measurement volume can interfere with its velocity measurements (Berg et al., 2016). We examined the effect of sensor proximity to the measurement volume on the signal amplitude of the ADV in a tank of filtered water. Based on those measurements, we aligned the pH intake tube 2.6 cm from the edge of the measurement volume, and the tip of the O_2 sensor 1.8 cm from the edge of the measurement volume.

In benthic flux measurements, the footprint of the technique is defined as the minimum area of the seafloor that contributes 90% of the eddy covariance flux signal. It is a narrow ellipse whose dimensions are a function of the sediment roughness parameter (z_0) and the height of the measurement volume above the bed (Berg et al., 2007). We determined the friction velocity during northward flow over undisturbed sediments, according to (Stull, 2012) as

$$u_* = \left(\overline{u_x' u_z'}^2 + \overline{u_y' u_z'}^2\right)^{1/4} \quad (3)$$

where the x, z, and y subscripts refer to longitudinal, transverse, and vertical components of velocity direction. For this analysis, we double-rotated the velocity field of a few half-hour time intervals when flow was northward (not-influenced by the experimental site) and the signal-to-noise ratio was high. Double-rotation aligned the primary axis of the velocity field with flow direction during the interval. This reduces the net transverse and vertical flow during each interval to zero. At a mean longitudinal velocity of 0.15 m s^{-1}, u_* was 0.0116 m s^{-1}. We then calculated z_0 using the law of the wall as

$$z_0 = \frac{h}{\exp\left(\frac{U_x \kappa}{u_*}\right)} \quad (4)$$

where h is the measurement height above the seafloor, U_x is the mean longitudinal velocity, and κ is the von Karman constant (equal to 0.41). At U_x equal to 0.15 m s^{-1} (and h equal to 0.16 m) z_0 was 7.6×10^{-4} m. Based on this measurement, the approximate area of the seafloor footprint was 30 m^2 (according to Berg et al., 2007). The predicted major and minor axes of the footprint ellipse were 35 m and 1.0 m, respectively. The point of maximum contribution to the flux signal was expected to be just 1.6 m upstream of the sensors.

We report the proton flux calculated from pH eddy covariance measurements as a DIC flux. The amount of CO_2 (g) dissolution required to generate the observed proton flux was calculated using the software CO_2SYS (Lewis and Wallace, 1998). For CO_2SYS calculations, the seawater carbonate chemistry was constrained with measurements of pH and total alkalinity by spectrophotometric lab-on-chip sensors (Schaap et al., 2021). Additional sensors on the instrument frame included galvanic oxygen and glass electrode pH (RBR, Inc. Canada). These were also positioned to sense concentration at a height of 16 cm above the bed. Weight restrictions on the ROV limited batteries on the instrument frame; the instruments could only measure continuously for 60 h. To make near-continuous measurements of the DIC flux over the eleven days of the experiment, two identical landers were used. As one lander was retrieved from the seafloor, a second lander was positioned in its place.

The velocity, pH, and oxygen time series, recorded at 16 Hz by the ADV, were downsampled to 5 Hz, the frequency of optode data collection. Eddy covariance fluxes were calculated in half-hour intervals following the procedure described by Holtappels et al. (2013). The tilt of the ADV was corrected using the planar fit method by Wilczak et al. (2001). A running average with a window length of 300 s was subtracted from the time series to calculate the fluctuating vertical velocity (u_z') and concentration (c').

2.3. DIC concentration at carbonate system equilibrium

To quantify CO_2 emission, we accounted for the kinetics of CO_2 equilibration. The kinetics of CO_2 equilibration are limited by the relatively slow reactions of the hydration and hydroxylation of CO_2 to HCO_3^-(Zeebe and Wolf-Gladrow, 2001). The equilibration time (t), defined as the time required for the carbonate system to reach 63% of equilibrium after a perturbation, is pH-dependent. As the equilibrium pH decreases, the equilibration time also decreases. To solve for the pH-dependent carbonate system equilibration time we used the complete equations presented in Schultz et al., (2006), to which we added two equations to account for its dependency on boron (Zeebe and Wolf-Gladrow, 2001). The equations were solved simultaneously using the Matlab® ODE solver. These calculations, including minor corrections to typos in prior work, are presented in Gros et al. (2021, Supplementary materials). At background pH (8.04) the equilibration time was 117.9 s. With the addition of 184 μmol L^{-1} of DIC, the equilibrium pH was 7.45 and the equilibration time decreased to 85.5 s.

To calculate the concentration of excess DIC (i.e., elevation of DIC above background) at chemical equilibrium, we iteratively solved for the pH-dependent equilibration time. First, we estimated the excess hydrogen ion concentration at equilibrium ($\delta[H^+]_{eq.}$). This calculation made use of the excess hydrogen ion concentration at time t according to kinetics presented by Zeebe and Wolf-Gladrow (2001) as

$$\delta[H^+]_{eq} = \frac{\delta[H^+]_t}{(1 - e^{-it})} \quad (5)$$

where t is the sum of the time delay due to transport from the bubble streams to the instruments and any time required for measurement. For the first calculation, we assumed that $\tau = 117.9$ s. We then used the resulting $\delta[H^+]_{eq}$ to calculate a new τ, according to the paragraph above. We iterated this sequence of calculations until the $\delta[H^+]_{eq}$ no longer changed between iterations. We then used CO_2SYS (Lewis and Wallace, 1998) to calculate the enrichment of DIC above background concentration at equilibrium (δDIC_{eq}) from $\delta[H^+]_{eq}$. Alkalinity was 2319 μmol kg^{-1} (Esposito et al., 2021; Schaap et al., 2021). Our calculations were simplified by the observation that there was no alkalinity signal in the water column plume (Schaap et al., 2021).

2.4. Quantification of total CO_2 emitted

To determine CO_2 emission during the release experiment we relied on five sources of data. The first data source, eddy covariance instruments, provided time series measurements of pH, current velocity and current direction. The second data source, lab-on-chip pH sensors were used to calibrate eddy covariance pH (details in Section 2.2), and to quantify the mean vertical δDIC distribution in the plume of aqueous CO_2 generated by bubble dissolution at the maximum injection rate (details Section 3.3). Third, the predicted vertical distribution of δDIC was determined with complementary numerical models of CO_2 (g) dissolution and its dispersion (details in Section 2.5). Fourth, the distance to the center of the bubble streams was determined from ROV observations. Finally, the mean bubble diameter emerging from the seafloor was needed for model predictions.

The current direction at the release site was tidally driven in a counterclockwise motion. We divided the time series into half-hour intervals to represent separate segments of the plume. We calculated the amount of CO_2 emitted in each segment as

$$DIC_n = \int_{seafloor}^{open\ \ water} w_n \cdot \delta DIC_n(z) \cdot U_n(z)\, dz \quad (6)$$

where n refers to a segment of the plume, w is the segment width determined as a perimeter of an arc defined by the initial and final current directions during the interval, $\delta DIC(z)$ is DIC enrichment above background concentration, at equilibrium, as a function of height above the seafloor, and $U_n(z)$ is the mean velocity magnitude (with x and y components) as a function of height above the seafloor. In detail, w was calculated as $(\theta_1\text{-}\theta_2)\cdot r$, where θ_1 is the mean x-y angle of flow direction at the beginning of the interval, θ_2 is the angle at the end of the interval, and r is the radius of the implied circle. In this case, r is the distance to the primary bubble stream (2.6 m). This was the approximate distance to the center of bubble streams throughout the experiment. Bubble stream locations and their intensity were determined from photographs and video imagery of the seafloor collected by the ROV during the experiment (Flohr et al., 2021b). The DIC concentration at the height of the measurement volume was calculated as described in Section 2.3. To quantify the vertical distribution of DIC, and to investigate changes in DIC flux with distance to the plume, we used two complementary numerical models. Details are provided in Section 2.5. To quantify the vertical distribution of U_n we applied the law of the wall to the mean velocity determined at the height of the ADV measurement volume. This calculation relied on the roughness parameter calculated in Eq. (4). DIC advection in the plume was then calculated as

$$DIC\ plume = \sum_{n} DIC_n. \quad (7)$$

2.5. Prediction of dDIC distribution using numerical models

Complementary numerical models were used to estimate the vertical distribution of DIC, and to determine DIC flux as a function of distance to the bubble streams. The first model was based on the two-phase plume model by Dewar et al. (2015). This model predicts the bubble rise height and rise velocity through a momentum balance, with the gas buoyancy counteracted by the drag encountered between the bubbles and the surrounding waters. The dissolution and distribution of DIC is predicted through a mass transfer correlation based on the bubble size, shape, and rise velocity, and the local seawater properties (i.e., pressure and temperature). The vertical DIC distribution was calculated for emerging bubbles with a mean diameter of 7 mm and a volume median diameter of 10.2 mm (determined from back-lit video imagery collected by a purpose-built lander positioned over the bubble stream on 15 May 2019 (Li et al., 2021). The second model calculated the effect of advection and dispersion on the resulting vertical distribution of DIC during its transport from the bubble-stream to the sensors. It was developed using Comsol Multiphysics® (Comsol Inc., Sweden). Specifically, we used a low Reynolds number k-ε turbulence model, coupled to the Transport of Dilute Species module. A detailed description of the underlying equations for turbulent transport, kinetic energy, its dissipation, and damping functions is provided in Holtappels et al. (2013). Briefly, the model we constructed was 12 m long in the direction of flow (x), 3 m wide (y) and 6 m tall (z). At the bottom face, we introduced an upward flux of DIC of 10 mmol $m^{-2}\ d^{-1}$, consistent with benthic biotic production. The top ($z = 6$ m), left ($y = 3$ m), and downstream ($x = 12$ m) faces of the model were open boundaries. The right face ($y = 0$ m) was used to represent the plume and the flow path directly downstream of it. Plume-derived DIC was introduced through a narrow rectangle (0.2 m wide, 4.5 m long) on this face according to the predictions of the two-phase model. The rectangle rose at a 45-degree angle from the bottom ($z = 0$) to a height of 3.2 m, above which the two-phase model predicted CO_2 (g) dissolution would be minimal. The rise angle accounted for downstream transport of the bubbles. The remainder of the right face was assigned a symmetry condition. To accurately represent turbulence and flow we used z_0 and u_* calculated from ADV measurements at the seafloor as described above.

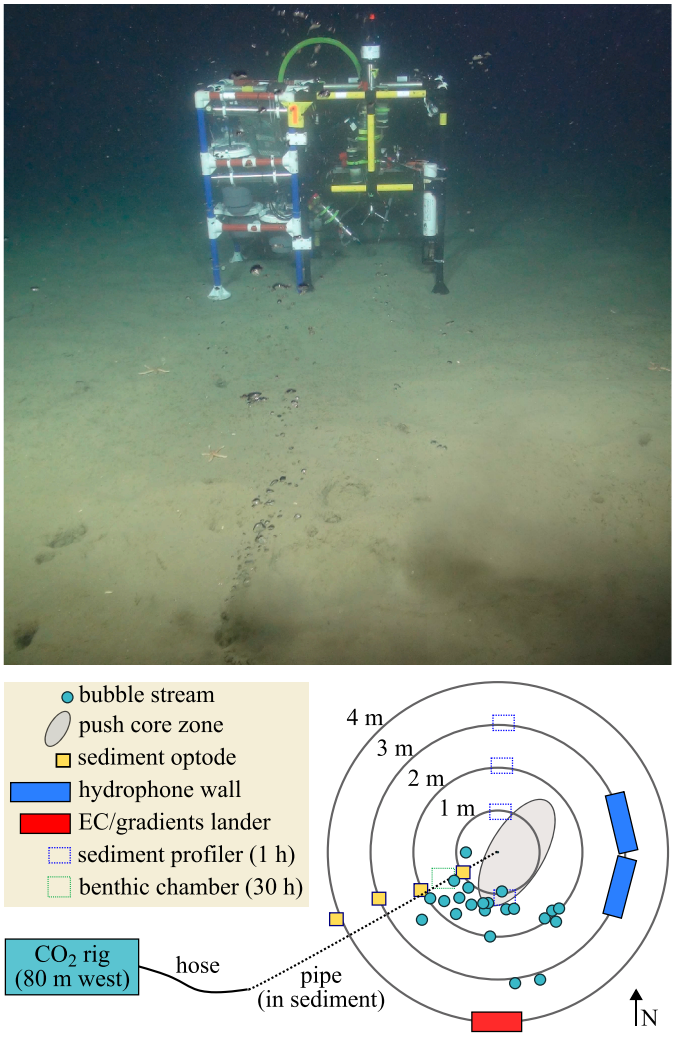

Fig. 2. The release experiment site. Top) Eddy covariance instruments and lab-on-chip sensors positioned a few meters to the south of CO_2 bubble streams on day 10 of the release experiment (21 May 2019, injection rate of 143 kg d^{-1}). Bottom) Schematic of instrument arrangement at the site modified from Flohr et al., (2021). The EC/gradients lander (red) is the eddy covariance and lab-on-chip lander.

3. Results

3.1. Leak detection with pH eddy covariance

CO_2 release commenced on 11 May 2019. As the ROV returned to the release site after opening the valves of the CO_2 container, it observed the first three CO_2 bubble streams. The most active bubble stream was located 2.6 m to the north of the eddy covariance lander. As the injection rate increased, the number of bubble streams and their areal distribution increased. Bubble streams primarily formed along a 2.5 m-wide east-west axis centered on the original active one. An exception was a bubble stream that emerged just one meter to the north of the eddy covariance lander at the end of day 6. Its flow diminished at the peak injection rate on day 9. An image of the eddy covariance lander position relative to the dominant bubble streams on the final day of the experiment is provided (Fig. 2). By the final day, there were nine active bubble streams, two intermittent streams, and ten sites of formerly active bubble streams. Thus, there was high variability in the locations of bubble stream emission during the experiment.

The dissolution of CO_2 (g) caused a vertical, turbulent pH flux that was detected by eddy covariance instruments at the lowest release rate and throughout the experiment (DIC flux; Figs. 3, 4). The elevated DIC flux was detected on the southward portion of tidally-oscillating flow, when the instruments were exposed to the low-pH plume of the CO_2 bubble streams. At the lowest injection rate, the peak DIC flux observed in the plume of the bubble streams (> 0.020 kg m^{-2} d^{-1}) was approximately 20x the background flux (< 0.001 kg m^{-2} d^{-1}; Fig. 3). As the experimental injection rate increased, the peak DIC flux increased (Fig. 4). At the peak injection rate of 143 kg d^{-1} the peak DIC flux was 0.5 kg m^{-2} d^{-1}. This is 500x the background flux, demonstrating that at close proximity, eddy covariance is remarkably sensitive to this introduced source of CO_2.

Naively, one might expect to observe an eddy covariance DIC flux of the rate of injection divided by the area of emission. At the peak injection rate of 143 kg d^{-1}, the bubble streams could be contained within a circle with a radius of 1.75 m. This is an area of 9.6 m^2, giving a first-order predicted emission of 14.9 kg m^{-2} d^{-1} (143 kg d^{-1} divided by 9.6 m^2). Instead, we observed a mean DIC flux of 0.06 kg m^{-2} d^{-1} when the instruments were downstream of the bubble streams (Fig. 4). A combination of factors contributes to this small flux. First, we can expect that a significant fraction of the injected CO_2 was retained by sediments (see Section 4.4). Second, of the CO_2 (g) that is emitted to the water column, much of it dissolves above the measurement volume of the eddy covariance instruments and therefore remains undetected by eddy covariance (Dewar et al., 2015; Gros et al., 2021). Third, the footprint of the eddy covariance technique is long, narrow, and larger than the area over which CO_2 emission occurred. Finally, the low pH plume generated by CO_2 bubble dissolution was likely not at chemical equilibrium due to the close proximity of instruments to the bubble streams (see Section 3.4).

3.2. Biotic CO_2 (aq) production and O_2 uptake

The pH eddy covariance technique was sensitive enough to quantify the pH flux that results from biological CO_2 production in seafloor sediments at the site. For these measurements we examined pH flux during northward flow, when the eddy covariance footprint was entirely upstream of the bubble streams. We collected the highest quality fluxes (i.e., fluxes with the most consistent flux signal) on day ten of the release experiment. The mean biological DIC efflux matched the mean O_2 uptake determined at the same time (Fig. 5). Differences between biological O_2 uptake and DIC production were not statistically significant (ANOVA, $\alpha = 0.05$), but both fluxes were significantly different from zero (one-sample t-tests, $\alpha = 0.05$). ROV disturbance of sediments on the south side of the lander during lander deployment and retrieval may have contributed to noise in the flux signal, but not all of the variation in biotic flux was noise. The magnitude of oxygen uptake and DIC production increased with increases in velocity (e.g., Fig. 5 at day 10.3). Benthic heterotrophic respiration is ultimately limited by organic matter delivery and its quality (Arndt et al., 2013). Over short time-scales, however, respiration may be enhanced by increases in oxygen supply from overlying water. Increases in velocity can also lead to increases in solute exchange. For these reasons, tidally driven oscillations in oxygen uptake occur in cohesive sediments (e.g., Donis et al., 2016; Glud et al., 2016; Koopmans et al., 2021). Further research is needed, but our results suggest that biotic DIC fluxes are similarly enhanced over short time scales by increases in water velocity.

The high sensitivity of the eddy covariance technique results from the covariance of high frequency velocity and pH signals. The covariance is illustrated in Fig. 6. At the peak injection rate, pH decreases greater than 0.03 units occurred roughly every four seconds in the plume of aqueous CO_2 generated by the experimental injection. Decreases in pH commonly occurred with an upward vertical velocity. The converse was also common. Both cases result in a net upward flux of hydrogen ions. Thus, both cases contribute to calculated DIC flux (Eqn. (1)). The covariance of vertical velocity and pH shows that the high frequency variations are a flux signal, not noise.

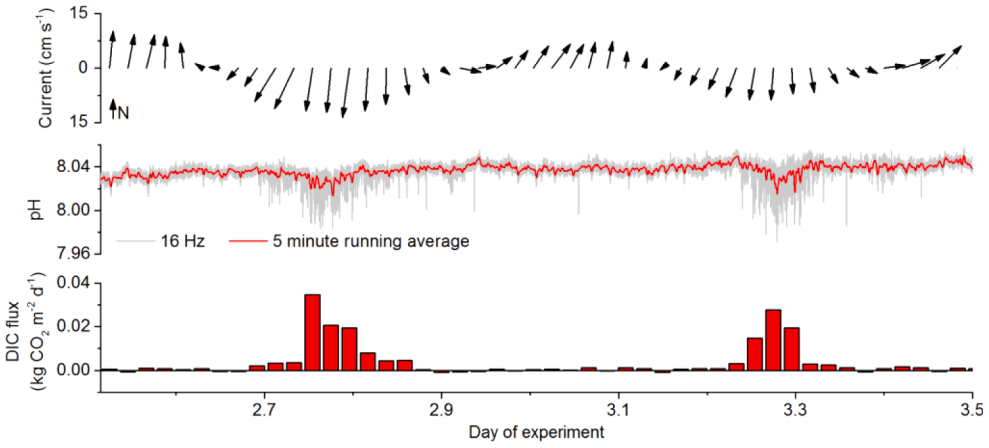

Fig. 3. Detailed view of the detection of CO_2 (g) dissolution (DIC flux) at the lowest injection rate (5.7 kg d^{-1}). Top) Current magnitude and direction with respect to north. Center) High frequency and time-averaged eddy covariance pH measurements. Bottom) DIC flux calculated from eddy covariance pH flux. Throughout this manuscript DIC flux is reported in kg of CO_2 for comparison with CO_2 injected.

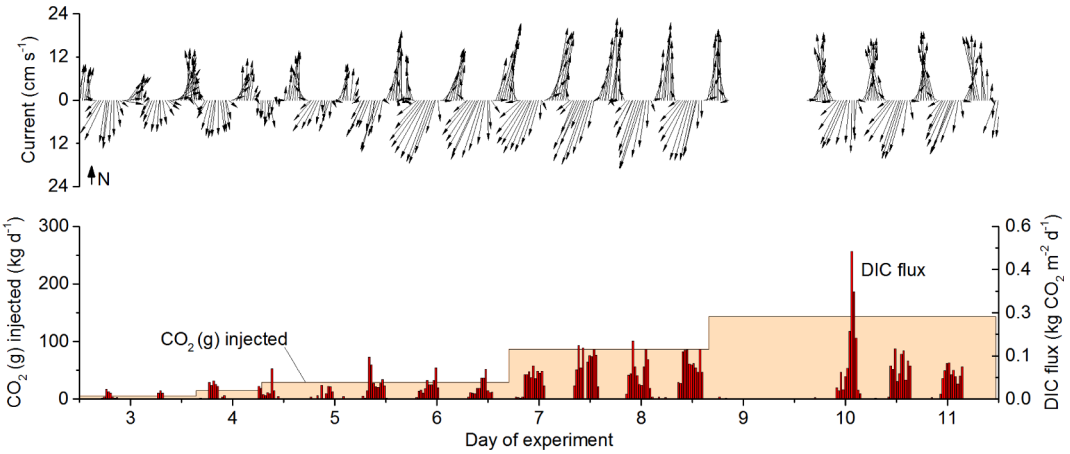

Fig. 4. DIC flux calculated from eddy covariance pH flux during the release experiment. Top) Current magnitude and direction with respect to north. Bottom) DIC flux and the experimental CO_2 (g) injection rate. The gap in current and DIC flux at day 9 was due to biofouling. Note that fluxes on days 2 and 3 are also presented in Fig. 3.

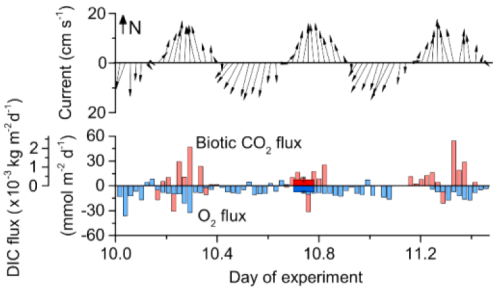

Fig. 5. Benthic biological DIC production and O_2 uptake determined by pH and O_2 eddy covariance on day 10 of the release experiment. DIC production (± SE) was 7.6 ± 3.2 mmol m^{-2} d^{-1}, $n = 36$. Eddy covariance O_2 uptake was 7.4 ± 1.3 mmol m^{-2} d^{-1}; $n = 60$.

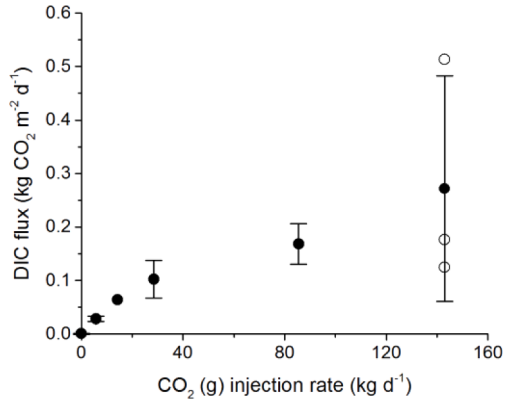

Fig. 7. The peak eddy covariance DIC flux (mean ± *s*.d.) in the plumes of the bubble streams. The three obervations of peak flux at the peak injection rate are shown (open circles). Biotic CO_2 production is represented at an injection rate of zero.

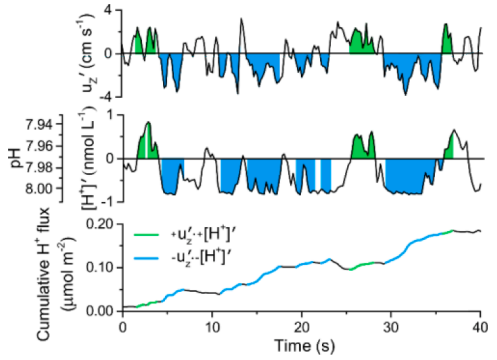

Fig. 6. Example of the covariance of turbulent vertical velocity and [H^+] that gives eddy covariance its high sensitivity. Top) The turbulent, fluctuating component of vertical velocity. Center) The turbulent, fluctuating component of [H^+]. Bottom) Cumulative flux contributions occur almost continuously in the plume of the bubble stream (day 10).

3.3. *DIC flux as a function of injection rate*

The peak eddy covariance DIC flux in the plume of the bubble streams did not increase linearly with the injection rate (Fig. 7). At injection rates above 20 kg d^{-1}, the additional CO_2 injected resulted in smaller increases in DIC flux. An exception is one observation at the highest injection rate. At this time, the peak DIC flux varied up to four-fold during the 13 h elapsed from one observation of the plume to the next. The diminished response above 20 kg d^{-1} was caused by the increasing area and number of bubble streams through which CO_2 emission occurred at the higher injection rates. Only a subset of the bubble streams would contribute to measured eddy covariance fluxes at any one time. The high variability in flux at the highest injection rate was likely due to intermittent CO_2 emission by the closest bubble streams.

To quantify the effect of bubble stream proximity on DIC flux, and to examine the vertical and horizontal distribution of bubble-derived DIC, we used complementary numerical models. The two-phase model predicted that the maximum rate of CO_2 (g) dissolution occurred just above the seafloor (Fig. 8A). This is where the volume of CO_2 (g) is at a maximum. The predicted rate of CO_2 (g) dissolution diminished near-linearly with height and, for a mean initial bubble diameter of 7 mm, was negligible at heights of greater than 4 m. The vertical profile of water velocity is inverted relative to this, with minimal velocity and minimal turbulent mixing near the bed. As a result, the advection-dispersion model predicted that DIC enrichment would be close to its maximum near the height of our instruments (0.16 m; the lower of the observation points in Fig. 8B). Lab-on-chip measurements of the vertical pH gradient at two points (0.16 m and 0.88 m) revealed a steeper mean gradient at the maximum release rate than predicted by our models. The cause may be an underestimation of the abundance of small bubbles (e.g., < 2 mm diameter), which would dissolve at a low height, enriching

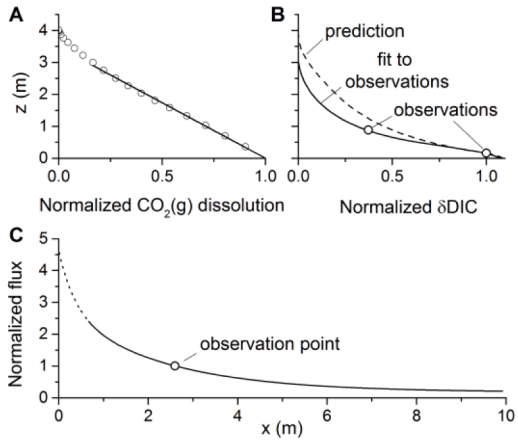

Fig. 8. Model prediction of A) the dissolution of CO_2 (g) by bubbles during this experiment, and B) the resulting vertical gradient in excess DIC at the instrument location fit to lab-on-chip pH observations. C) Prediction of DIC flux with distance downstream of a bubble stream. The modeled measuring height was 0.16 m. Flux is less predictable at the bubble stream (dotted line).

δDIC near the seafloor. Underestimation of small bubble sizes, along with coalescence and breakup of bubbles at low depths, make in situ bubble measurement challenging (Sellami et al., 2015). To improve the accuracy of our quantification of the vertical DIC profile, we fit our prediction to the observed concentration gradient (Fig. 8B). The resulting gradient is similar to one predicted by the emergence of bubbles with a mean diameter of 4 mm (Schaap et al., 2021).

The advection-dispersion model predicted that our measured eddy covariance DIC flux would depend on the distance to a bubble stream (Fig. 8C). At a distance of 1 m, the flux would be twice as great as at 2.6 m. Therefore, the temporary appearance of a bubble stream close to the instruments can explain the high variance in eddy covariance DIC flux at the peak injection rate Fig. 7. This model suggests that eddy covariance instruments would need to be located close to the bubble streams (i.e., within 10 m) in order to detect the smallest release rate in this study.

3.4. Equilibrium of the carbonate system

We found a substantial discrepancy between eddy covariance pH and lab-on-chip pH in the plume of the bubble streams. At the peak injection rate, the eddy covariance pH sensor and an accompanying glass pH electrode both reported a mean pH of 8.01 during southbound currents. The lab-on-chip pH sensor, measuring at the same height and on the same frame, reported a mean pH of 7.83 (e.g., Fig. 9A). The difference was due to incomplete chemical equilibration of CO_2. According to our calculations the equilibration time of the carbonate system was 117.9 s (at pH 8.04, 7.8 °C). At a mean water velocity in the plume of 11 cm s^{-1}, and a distance of 2.6 m between the bubble streams and the instruments, the eddy covariance sensor and glass electrode would have detected the pH signal of CO_2 dissolution 24 s after the CO_2 bubble emerged from the sediment. This short time would allow for only 18% of CO_2 hydration/hydroxylation and proton production (Eq. (6)). In contrast to the eddy covariance sensor, the lab-on-chip sensor includes an average time-lag of 140 s between sample collection and analysis. Because of this, lab-on-chip pH would have been determined at 70% of chemical equilibrium.

For this study, we used pH observations made during eddy covariance pump reversals to determine δDIC at chemical equilibrium. Lab-on-chip pH measurements were unavailable for this because they are the subject of a companion manuscript (Schaap et al., 2021). During standard eddy covariance measurements, inflowing water passes the ISFET sensor and travels through 6 cm^3 of tubing on route to a 550 cm^3 filter housing that traps sand before reaching the gear pump. During the

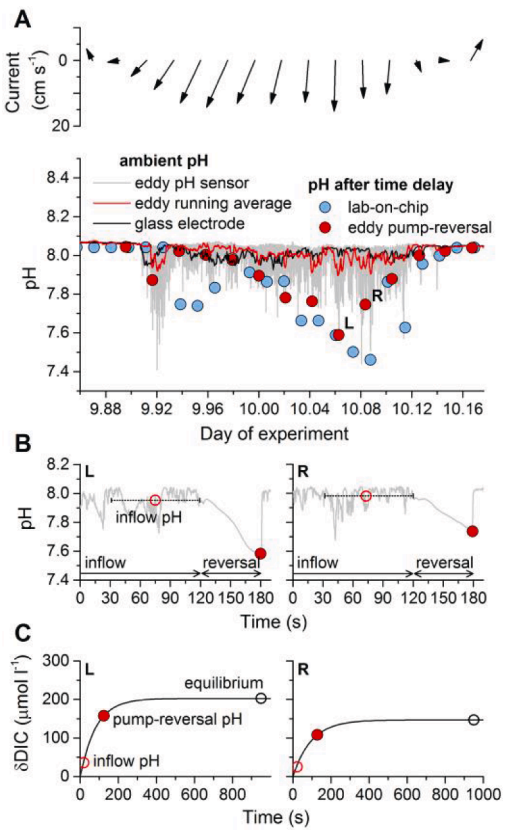

Fig. 9. Disequilibrium of carbonate chemistry in the plume of the bubble streams at the peak CO_2 injection rate. A) pH determined by sensors that briefly retained a water sample prior to analysis observed a lower pH. B) Pump-reversal pH measurements on the same parcel of water during inflow (90 s running average) and at the end of the reversal at points L and R in panel A. C) δDIC at inflow pH, pump-reversal pH, and at chemical equilibrium at points L and R in panel A.

one-minute-long reversal, 150 cm^3 of this water are discharged backwards past the ISFET sensor, providing a second pH measurement. This temporary storage of water brings the carbonate system closer to chemical equilibrium. The pH of discharging water in the final seconds of pump reversal, hereafter referred to as the pump reversal pH, was similar to observations of pH detected by the lab-on-chip sensor (Fig. 9A). At the peak injection rate, the mean pump reversal pH in the plume of the bubble stream was 7.86, close to the mean LOC pH of 7.83. Outside of the plume, the pump reversal pH matched the background (8.04), indicating that the reduced pH detected in the plume was due to CO_2 (g) dissolution caused by the bubble streams. We used the successive measurements (inflow and outflow) to constrain the transport time and residence time of water in the system. We found the best fit of mean residence time of water in the system (data not shown) was 105 s (the midpoint of inflow pH shown in Fig. 9B). We then used pump reversal pH to calculate δDIC at equilibrium (Fig. 9C).

3.5. Quantification of CO_2 (g) emission

Time series measurements of velocity and pH were used to calculate the transport of δDIC in narrow arc-lengths defined by half-hour measurement intervals according to Eq. (6). An illustration of the results of these calculations is presented in Fig. 10. The equilibrium δDIC content of the plume was highly heterogeneous in cross-section, with differences of 100 mmol δDIC L^{-1} separated by tens of centimeters. Based on our calculations of chemical equilibrium, 73 ± 13% (mean ± *s*.d.) of CO_2 was emitted to overlying water at the peak injection rate (Fig. 11). Uncertainty in these measurements is the normalized s.d. of emission at

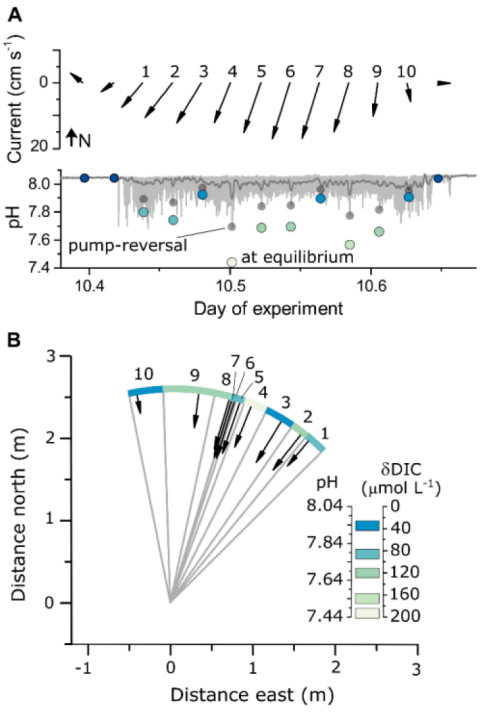

Fig. 10. Example calculation of plume δDIC transport. A) Time series of current magnitude, direction, and pH determined by the eddy sensor during inflow (light gray, with 5-minute running average in dark gray), during pump-reversal, and at chemical equilibrium. B) The resulting δDIC distribution and transport in cross-section.

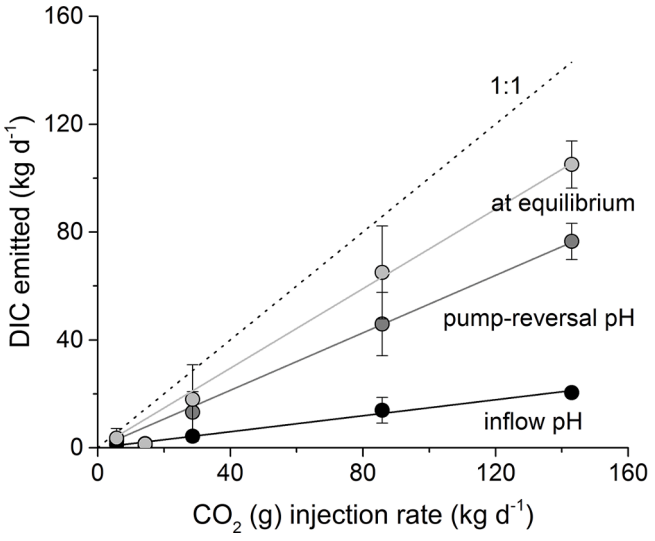

Fig. 11. CO_2 emission during the release experiment. Emission was determined from the eddy pH sensor during inflow (closed circles, ± *s*.d.; fit represents 15% of injected CO_2), during pump-reversal (dark gray; 53% of injected CO_2), and at the calculated chemical equilibrium (light gray; 73 ± 13% of injected CO_2).

injection rates of 88 and 143 kg d^{-1}. If we disregard chemical equilibrium and base our calculations of emission on pH measured during inflow, the calculated emission was one-fifth of this. Therefore, to accurately determine CO_2 emission close to a bubble stream, the equilibration of the carbonate system must be accounted for.

4. Discussion

4.1. Leak detection with pH eddy covariance

Our results demonstrate that pH eddy covariance is an effective technique for detecting extremely small CO_2 leaks from the seafloor. The limit of detection in other settings would depend on distance to the leak, instrument height, and water depth, among other factors. However, we unambiguously detected CO_2 (g) bubble dissolution at the lowest injection rate of 5.7 kg d^{-1} (Fig. 3). We were also able to quantify biotic CO_2 (g) emission (Fig 5). Active acoustic techniques are a highly effective technology at bubble detection, and are currently in use for monitoring of offshore CCS sites. We suggest that pH eddy covariance could be useful in a complementary monitoring role because of its high sensitivity and chemical specificity. A hypothetical application would be to discriminate methane from CO_2 bubble streams. Eddy covariance could also be used to detect dissolved CO_2 emission where bubbles are absent, such as at great depth. Among the restrictions on the use of eddy covariance in these roles is a requirement that the instruments may need to be within 10 m of the source to detect small leaks (e.g., 5.7 kg d^{-1}; Fig. 8). The point of maximum contribution to eddy covariance flux during typical deployments is within 1–2 m of the instruments (Berg et al., 2007; Rodil et al., 2019). In this respect, while eddy covariance appears to be more sensitive at leak detection than other geochemical techniques, it may not substantially extend the expected distance to which a CO_2 bubble stream could be detected by geochemical techniques. This limitation of proximity could be overcome by mounting eddy covariance instruments to an autonomous underwater vehicle. Aquatic eddy covariance has previously been determined from a moving platform (Berg et al., 2020; Flügge et al., 2016; Long and Nicholson, 2018). Therefore, the method is feasible. Alternately, pH eddy covariance could be used to monitor a location at risk of leakage, such as at a well-head.

4.2. Importance of equilibration of carbonate chemistry

The difference in DIC emission calculated at the pH of inflow and at chemical equilibrium (Fig. 11) demonstrates the importance of accounting for chemical equilibrium when measuring CO_2 emission close to a bubble stream. At the temperature of the experimental release site, and at a mean water velocity of 11 cm s^{-1}, the carbonate system would be at only 79% of equilibrium at a distance of 20 m (calculated following Eq. (5), where τ is 117.9 s). Therefore, to a measurement distance of tens of meters, the effect can be significant. The time to equilibration diminishes rapidly as temperature increases. At 16 °C, for example, τ is less than 50 s. Therefore, at higher temperatures this effect would be less of a concern.

4.3. Biotic CO_2 (aq) production and O_2 uptake

During measurements of biotic CO_2 production using the pH eddy covariance technique, biogeochemical processes other than CO_2 (g) dissolution may contribute to proton flux. In broad terms, sediment pH is driven by aerobic and anaerobic organic matter mineralization as well as calcium carbonate dissolution and precipitation (reviewed by Burdige, 2006). A simplifying observation is that whether the perturbance of the carbonate system is due to production of protons or production of CO_2, the equilibration of the carbonate system drives an equivalence between them, such that a proton flux represents a net CO_2 flux (see eqn. (1)).

We suggest that disequilibrium of carbonate chemistry is not an issue for calculations of benthic, biological (biotic) CO_2 production. A fraction of benthic biotic CO_2 production may escape detection in pH eddy covariance measurements because it has not yet hydrated/hyroxylated in water, i.e., it was produced within 2–3 min of it passing across the face of the pH sensor. A complete analysis is beyond the scope of this work,

but we suggest that the fraction that escapes detection is too small to alter our calculated biotic CO_2 emission. Diffusive transport times for solutes through sediments and the diffusive boundary layer can be calculated according to (Jørgensen and Revsbech, 1985) as

$$t = \frac{z^2}{0.9D} \quad (9)$$

where z is the diffusion distance, and D is the molecular diffusivity (10^{-5} $cm^2\ s^{-1}$ for CO_2 at 8 °C). For CO_2 produced just below the sediment surface the diffusion distance might be just 400 μm (e.g., 100 μm of pore space and 300 μm of diffusive boundary layer at the sediment-water interface). In this case, the diffusive transport time would be 141 s. If this occurred in sediments close to the eddy covariance instruments the turbulent transport time could be as short as 10 s. The diffusive and turbulent transport times would then add to 151 s. This minimal transport time allows 72% of CO_2 to hydrate/hydroxylate prior to measurement (*Eq. (5)*). The vast majority of benthic, biotic CO_2 production occurs at greater depths than this (e.g., Jørgensen, 1982), and diffusive transport time increases with z^2 (*Eq. (9)*). Therefore, in most cases, benthic, biotically produced CO_2 would equilibrate in water prior to passing across an eddy covariance sensor.

Biotic CO_2 production in sediments, calculated from H^+ flux, was similar to O_2 uptake (Fig. 5). Generally, one would expect CO_2 production to match O_2 uptake during organic matter mineralization in marine sediments. This is because processes that consume oxygen without producing CO_2 tend to be offset by processes that produce CO_2 without consuming oxygen. Specifically, the oxidation of non-carbon elements in organic matter consumes additional oxygen. This oxygen consumption is often offset by denitrification and iron pyrite formation in which N_2 and FeS_2 are the ultimate electron acceptors (Glud, 2008). $CaCO_3$ production or dissolution in sediments can substantially alter this ratio. $CaCO_3$ dissolution is a source of CO_2 but a sink for H^+. For our H^+ flux measurements, net $CaCO_3$ dissolution in sediments would diminish our calculated CO_2 emission. In the silicate sediments at the experimental release site, however, net $CaCO_3$ production or dissolution was minimal (Dale et al., 2021).

4.4. Quantification of CO_2 (g) emission

In terrestrial CCS, eddy covariance has been used to quantify experimental CO_2 release (Lewicki and Hilley, 2009; Lewicki et al., 2010). Those studies relied on a more advanced approach for quantification, a least squares inversion of footprint functions. In our study, we were fortunate that the regular, counterclockwise progression of current directions, and the rapid dissolution of CO_2 into water allowed us to constrain plume dimensions from measurements taken at a single point. Among the limitations of our approach is that the distance to the bubble stream determines at a ratio of 1:1 the transverse dimension (w_n) of the plume, and therefore its magnitude. Our measurement of CO_2 emission at the peak CO_2 (g) injection rate (73 ± 13%) indicates that 27% of the injected CO_2 (g) was retained in sediments at that time. A total of 675 kg of CO_2 were injected during the experiment. If we apply the 27% loss rate to the whole experiment, then 183 kg were retained in sediments during this experiment. Given that the depth of the diffuser was only 3 m, the results suggest that sediments were a very effective sink for CO_2 (g). Companion studies suggest that much of the lost CO_2 was dissolved in porewater. Evidence for this includes a 0.5 °C temperature increase at 10 cm depth in the vent area due to CO_2-induced carbonate and silicate mineral dissolution (de Beer et al., 2021). Alkalinity accumulated in sediments as a result of this dissolution (Lichtschlag et al., 2021) showed evidence of gas pockets within the sediments (Roche et al., 2021). These results are consistent with substantial CO_2 loss to sediments in a similar experiment during which CO_2 was injected at greater depths at a nearshore marine site (Lichtschlag et al., 2015).

Our results compare favorably with measurements of CO_2 release to the water column made by other techniques during this experiment. In closely related work Schaap et al. (2021) used lab-on-chip sensors to quantify the vertical pH gradient every 20 min in the plume of aqueous CO_2 generated by the bubble streams. They found that after accounting for equilibration, 61 ± 10% of injected CO_2 was released to the water column at the peak injection rate. In another geochemical approach, Gros et al. (2021) used pCO_2 sensors mounted to a CTD to survey the plume of aqueous CO_2. They found that 64% of injected CO_2 was released to the water column at the peak injection rate. (Flohr et al., 2021a) quantified release to the water column by gas collection over bubble streams. They found that 38 ± 12% and 48 ± 7% of injected CO_2 were released to the water column during successive days at the peak injection rate. Finally, hydrophones were used to quantify CO_2 bubble emission from the "pop" sound they make as surface tension encloses a bubble on its emergence from the sediment (Li et al., 2021). They found that 22 ± 62% of injected CO_2 was released to the water column at the peak injection rate.

4.5. Anomaly attribution

Beyond leak detection and quantification, eddy covariance may be useful for attribution of leak-like pH signals in a seafloor CCS monitoring program. Geochemical leak detection has focused on identification of variations in pH with flow direction that can be indicative of a leak (e.g., Blackford et al., 2017; Oleynik et al., 2018). However, natural processes can also cause variations in pH with flow direction. Prior to the start of CO_2 injection in this study, tidally-oscillating pH variations of 0.01 unit were observed by lab-on-chip pH sensors at the release site (Schaap et al., 2021). These oscillations were caused by velocity-induced redistribution of the equilibrium pH profile in the benthic boundary layer. The effect of transient velocity on equilibrium dissolved oxygen profiles has been previously described (Holtappels et al., 2013). Stable stratification could also expose stationary sensors to variations in pH with flow direction. Similar oscillations in pH may also be caused by internal waves. In any of these cases, eddy covariance could improve attribution of anomalies like these by quantifying solute flux instead of solute concentration. Additionally, the abiotic or biotic origin of a CO_2 source can be determined by comparing eddy covariance oxygen uptake to DIC efflux. Where DIC efflux exceeds uptake, the source is abiotic. This work would complement other approaches that resolve the concentration changes of biologically-linked elements to identify anomalies caused by leaks (e.g., oxygen consumption; Botnen et al., 2015; Omar et al., 2021). Improved models of the physics, chemistry, and biological element cycling in seawater overlying offshore CCS sites would improve our understanding of these dynamics. Here, eddy covariance can also contribute by improving quantification of biotic fluxes and fluxes across pycnoclines (e.g., Kreling et al., 2014; Rovelli et al., 2016), improving the accuracy of models.

5. Conclusion

Eddy covariance may be useful for offshore CCS, including environmental monitoring, leak detection, attribution of leak-like signals, and quantification of CO_2 emission. The most remarkable attribute may be that because natural CO_2 production can be quantified with the technique, we can be confident that eddy covariance can detect small leaks (e.g., 5.7 kg d^{-1} in this study). The covariance of vertical velocity and pH makes the eddy covariance technique, in effect, an amplifier for the detection of CO_2 (g) dissolution at the seafloor. The combination of velocity and pH sensors can also be used to quantify the total CO_2 (g) emission from the seafloor using the plume advection approach that we demonstrated. For quantification, the distance to the source and an estimate of the distribution of CO_2 (g) dissolution with height would be needed. To be useful at leak-detection in CCS monitoring, the instruments could be placed to monitor at-risk locations such as a well head, or positioned on mobile platforms.

Declaration of Competing Interest

The authors declare that they have no known competing financial interests or personal relationships that could have appeared to influence the work reported in this paper.

Acknowledgements

The authors thank two anonymous reviewers for improving this manuscript. DK is grateful to Dirk de Beer (MPI-MM) for his support and guidance. The authors also thank the crews of the RRS James Cook, the R/V Poseidon, and the operations team responsible for the ROV ISIS. We also thank Ko-Ichi Nakamura of NIAIST in Tsukuba, Japan for guidance on ceramic membranes for the reference electrode. We also thank Andy Dale (GEOMAR) for helpful discussions, James Strong and Chris Pearce (NOC) for managing operations on the cruise, and Carla Sands (NOC). This project received funding from the European Union's Horizon 2020 research and innovation program under grant agreement No. 654462 (STEMM-CCS), it also received funding from the Max Planck Society and the Helmholtz Society. MHL was supported by US NSF grant # OCE-1657727.

References

Arndt, S., Jørgensen, B.B., LaRowe, D.E., Middelburg, J., Pancost, R., Regnier, P., 2013. Quantifying the degradation of organic matter in marine sediments: a review and synthesis. Earth Sci. Rev. 123, 53–86.

Beaubien, S., Jones, D., Gal, F., Barkwith, A., Braibant, G., Baubron, J.-C., Ciotoli, G., Graziani, S., Lister, T., Lombardi, S., 2013. Monitoring of near-surface gas geochemistry at the Weyburn, Canada, CO2-EOR site, 2001–2011. Int. J. Greenhouse Gas Control 16, S236–S262.

Berg, P., Koopmans, D.J., Huettel, M., Li, H., Mori, K., Wüest, A., 2016. A new robust oxygen-temperature sensor for aquatic eddy covariance measurements. Limnol. Oceanogr.: Methods 14, 151–167.

Berg, P., Long, M.H., Huettel, M., Rheuban, J.E., McGlathery, K.J., Howarth, R.W., Foreman, K.H., Giblin, A.E., Marino, R., 2013. Eddy correlation measurements of oxygen fluxes in permeable sediments exposed to varying current flow and light. Limnol. Oceanogr. 58, 1329–1343.

Berg, P., Pace, M.L., Buelo, C.D., 2020. Air–water gas exchange in lakes and reservoirs measured from a moving platform by underwater eddy covariance. Limnol. Oceanogr.: Methods.

Berg, P., Røy, H., Janssen, F., Meyer, V., Jørgensen, B.B., Huettel, M., de Beer, D., 2003. Oxygen uptake by aquatic sediments measured with a novel non-invasive eddy-correlation technique. Mar. Ecol. Prog. Ser. 261, 75–83.

Berg, P., Røy, H., Wiberg, P.L., 2007. Eddy correlation flux measurements: the sediment surface area that contributes to the flux. Limnol. Oceanogr. 52, 1672–1684.

Blackford, J., Alendal, G., Avlesen, H., Brereton, A., Cazenave, P., Chen, B., Dewar, M., Holt, J., Phelps, J., 2020. Impact and detectability of hypothetical CCS offshore seep scenarios as an aid to storage assurance and risk assessment. IJGGC 95.

Blackford, J., Artioli, Y., Clark, J., de L., Mora, 2017. Monitoring of offshore geological carbon storage integrity: implications of natural variability in the marine system and the assessment of anomaly detection criteria. Int. J. Greenhouse Gas Control 64, 99–112.

Blackford, J., Bull, J.M., Cevatoglu, M., Connelly, D., Hauton, C., James, R.H., Lichtschlag, A., Stahl, H., Widdicombe, S., Wright, I.C., 2015. Marine baseline and monitoring strategies for carbon dioxide capture and storage (CCS). Int. J. Greenhouse Gas Control 38, 221–229.

Blackford, J., Stahl, H., Bull, J.M., Bergès, B.J., Cevatoglu, M., Lichtschlag, A., Connelly, D., James, R.H., Kita, J., Long, D., 2014. Detection and impacts of leakage from sub-seafloor deep geological carbon dioxide storage. Nat. Clim. Chang 4, 1011–1016.

Botnen, H.A., Omar, A.M., Thorseth, I., Johannessen, T., Alendal, G., 2015. The effect of submarine CO2 vents on seawater: implications for detection of subsea carbon sequestration leakage. Limnol. Oceanogr. 60, 402–410.

Bresnahan Jr., P.J., Martz, T.R., Takeshita, Y., Johnson, K.S., LaShomb, M., 2014. Best practices for autonomous measurement of seawater pH with the Honeywell Durafet. Methods in Oceanography 9, 44–60. https://doi.org/10.1016/j.mio.2014.08.003.

Bui, M., Adjiman, C.S., Bardow, A., Anthony, E.J., Boston, A., Brown, S., Fennell, P.S., Fuss, S., Galindo, A., Hackett, L.A., 2018. Carbon capture and storage (CCS): the way forward. Energy Environ. Sci. 11, 1062–1176.

Burdige, D.J., 2006. Geochemistry of Marine Sediments. Princeton University Press.

CSLF, 2017. Practical Regulations and Permitting Process for Geological CO2 storage. Carbon sequestration leadership forum, p. 59.

Dale, A.W., Sommer, S., Lichtschlag, A., Koopmans, D., Haeckel, M., Kossel, E., Deusner, C., Linke, P., Scholten, J., Wallmann, K., van Erk, M.R., Gros, J., Scholz, F., Schmidt, M., 2021. Defining a biogeochemical baseline for sediments at Carbon Capture and Storage (CCS) sites: An example from the North Sea (Goldeneye). International Journal of Greenhouse Gas Control 106, 1–15. https://doi.org/10.1016/j.ijggc.2021.103265.

de Beer, D., Lichtschlag, A., Flohr, A., van Erk, M.R., Ahmerkamp, S., Holtappels, M., Haeckel, M., Strong, J., 2021. Sediment acidification and temperature increase in an artificial CO2 vent. Int. J. Greenhouse Gas Control 105, 103244.

Dean, M., Blackford, J., Connelly, D., Hines, R., 2020. Insights and guidance for offshore CO2 storage monitoring based on the QICS, ETI MMV, and STEMM-CCS projects. Int. J. Greenhouse Gas Control 100, 103120.

Dean, M., Tucker, O., 2017. A risk-based framework for Measurement, Monitoring and Verification (MMV) of the Goldeneye storage complex for the Peterhead CCS project. UK. Int. J. Greenhouse Gas Control 61, 1–15.

Delwiche, K., Hemond, H.F., 2017a. An enhanced bubble size sensor for long-term ebullition studies. Limnol. Oceanogr.: Methods 15, 821–835.

Delwiche, K.B., Hemond, H.F., 2017b. Methane bubble size distributions, flux, and dissolution in a freshwater lake. Environ. Sci. Technol. 51, 13733–13739.

Dewar, M., Sellami, N., Chen, B., 2015. Dynamics of rising CO2 bubble plumes in the QICS field experiment: part 2–Modelling. Int. J. Greenhouse Gas Control 38, 52–63.

Donis, D., McGinnis, D.F., Holtappels, M., Felden, J., Wenzhoefer, F., 2016. Assessing benthic oxygen fluxes in oligotrophic deep sea sediments (HAUSGARTEN observatory). Deep Sea Res. Part I 111, 1–10.

Esposito, M., Martinez-Cabanas, M., Connelly, D.P., Jasinski, D., Linke, P., Schmidt, M., Achterberg, E.P., 2021. Water column baseline assessment for offshore Carbon Dioxide Capture and Storage (CCS) sites: analysis of field data from the Goldeneye storage complex area. Int. J. Greenhouse Gas Control 109, 103344.

Feenstra, C., Mikunda, T., Brunsting, S., 2010. What happened in Barendrecht. Case study on the planned onshore carbon dioxide storage in Barendrecht, the Netherlands. Prepared by the Energy Research Centre of the Netherlands (ECN) Project 6.

Flohr, A., Matter, J.M., James, R.H., Saw, K., Brown, R., Ballentine, C.J., Day, C., Connelly, D., Flude, S., Gros, J., Hillegonds, D.J., Lichtschlag, A., Pearce, C.R., Peel, K., Strong, J., Tyne, R., 2021a. Utility of natural and artificial geochemical tracers for leakage monitoring and quantification during an offshore controlled CO2 release experiment. Int. J. Greenhouse Gas Control.

Flohr, A., Schaap, A., Achterberg, E.P., Alendal, G., Arundell, M., Berndt, C., Blackford, J., Böttner, C., Borisov, S.M., Brown, R., 2021b. Towards improved monitoring of offshore carbon storage: a real-world field experiment detecting a controlled sub-seafloor CO2 release. Int. J. Greenhouse Gas Control 106, 103237.

Flügge, M., Paskyabi, M.B., Reuder, J., Edson, J.B., Plueddemann, A.J., 2016. Comparison of direct covariance flux measurements from an offshore tower and a buoy. J. Atmos. Oceanic Technol. 33, 873–890.

Furre, A.-K., Eiken, O., Alnes, H., Vevatne, J.N., Kiær, A.F., 2017. 20 Years of Monitoring CO2-injection at Sleipner. Energy Procedia 114, 3916–3926.

GCCSI, 2019. Global Status of CCS 2019, Targeting Climate Change.

Glud, R.N., 2008. Oxygen dynamics of marine sediments. Marine Biology Research 4, 243–289. https://doi.org/10.1080/17451000801888726.

Glud, R.N., Berg, P., Stahl, H., Hume, A., Larsen, M., Eyre, B.D., Cook, P.L., 2016. Benthic carbon mineralization and nutrient turnover in a Scottish sea loch: an integrative in situ study. Aquat. Geochem. 22, 443–467.

Gros, J., Schmidt, M., Linke, P., Dötsch, S., Triest, J., Martínez-Cabanas, M., Esposito, M., Dale, A.W., Sommer, S., Flohr, A., 2021. Quantification of dissolved CO2 plumes at the Goldeneye CO2-release experiment. Int. J. Greenhouse Gas Control 109, 103387.

Holtappels, M., Glud, R.N., Donis, D., Liu, B., Hume, A., Wenzhöfer, F., Kuypers, M.M., 2013. Effects of transient bottom water currents and oxygen concentrations on benthic exchange rates as assessed by eddy correlation measurements. J. Geophys. Res.: Oceans 118, 1157–1169.

Holtappels, M., Noss, C., Hancke, K., Cathalot, C., McGinnis, D.F., Lorke, A., Glud, R.N., 2015. Aquatic eddy correlation: quantifying the artificial flux caused by stirring-sensitive O 2 sensors. PLoS ONE 10, e0116564.

IPCC, 2019. Global warming of 1.5 °C. An IPCC Special Report on the impacts of global warming of 1.5 °C above pre-industrial levels and related global greenhouse gas emission pathways, in the context of strengthening the global response to the threat of climate change, sustainable development, and efforts to eradicate poverty, in: V. Masson-Delmotte, P.Z., H. O. Pörtner, D. Roberts, J. Skea, P.R. Shukla, A. Pirani, W., Moufouma-Okia, C.P., R. Pidcock, S. Connors, J. B. R. Matthews, Y. Chen, X. Zhou, M. I. Gomis, E. Lonnoy, T. Maycock, M. Tignor, T. Waterfield (Eds.).

Jørgensen, B.B., 1982. Mineralization of organic matter in the sea bed—The role of sulphate reduction. Nature 296, 643–645.

Jørgensen, B.B., Revsbech, N.P., 1985. Diffusive boundary layers and the oxygen uptake of sediments and detritus 1. Limnol. Oceanogr. 30, 111–122.

Koopmans, D., Berg, P., Brunner, S., Val Klump, J., 2021. Seiche-and storm-driven benthic oxygen uptake in a eutrophic freshwater bay determined with aquatic eddy covariance. Freshwater Sci. 40, 259–273.

Kreling, J., Bravidor, J., McGinnis, D.F., Koschorreck, M., Lorke, A., 2014. Physical controls of oxygen fluxes at pelagic and benthic oxyclines in a lake. Limnol. Oceanogr. 59, 1637–1650.

Leighton, T., White, P., 2012. Quantification of undersea gas leaks from carbon capture and storage facilities, from pipelines and from methane seeps, by their acoustic emissions. Proc. R. Soc. A: Math. Phys. Eng. Sci. 468, 485–510.

Lewicki, J.L., Hilley, G.E., 2009. Eddy covariance mapping and quantification of surface CO2 leakage fluxes. Geophys. Res. Lett. 36.

Lewicki, J.L., Hilley, G.E., Dobeck, L., Spangler, L., 2010. Dynamics of CO 2 fluxes and concentrations during a shallow subsurface CO 2 release. Environ Earth Sci 60, 285–297.

Lewis, E., Wallace, D., 1998. Program developed for CO2 system calculations. Environmental System Science Data Infrastructure for a Virtual Ecosystem.

Li, J., White, P.R., Roche, B., Bull, J.M., Leighton, T.G., Davis, J.W., Fone, J.W., 2021. Acoustic and optical determination of bubble size distributions–Quantification of seabed gas emissions. Int. J. Greenhouse Gas Control 108, 103313.

Lichtschlag, A., Haeckel, M., Olierook, D., Peel, K., Flohr, A., Pearce, C.R., Marieni, C., James, R.H., Connelly, D.P., 2021. Impact of CO2 leakage from sub-seabed carbon dioxide storage on sediment and porewater geochemistry. Int. J. Greenhouse Gas Control 109, 103352.

Lichtschlag, A., James, R.H., Stahl, H., Connelly, D., 2015. Effect of a controlled sub-seabed release of CO2 on the biogeochemistry of shallow marine sediments, their pore waters, and the overlying water column. Int. J. Greenhouse Gas Control 38, 80–92.

Linke, P., Haeckel, M., Schneider von Deimling, J., Vielstädte, L., Schmidt, M., Karstens, J., Berndt, C., Herreilers, H., Lichtschlag, A., James, R., 2014. Fluxes of CO2 from natural seep sites and Sleipner storage site.

Long, M.H., 2021. Aquatic Biogeochemical Eddy Covariance Fluxes in the Presence of Waves. J. Geophys. Res.: Oceans 126, e2020JC016637.

Long, M.H., Charette, M.A., Martin, W.R., McCorkle, D.C., 2015. Oxygen metabolism and pH in coastal ecosystems: eddy Covariance Hydrogen ion and Oxygen Exchange System (ECHOES). Limnol. Oceanogr.: Methods 13, 438–450.

Long, M.H., Nicholson, D.P., 2018. Surface gas exchange determined from an aquatic eddy covariance floating platform. Limnol. Oceanogr.: Methods 16, 145–159.

Long, M.H., Sutherland, K., Wankel, S.D., Burdige, D.J., Zimmerman, R.C., 2020. Ebullition of oxygen from seagrasses under supersaturated conditions. Limnol. Oceanogr. 65, 314–324.

Oleynik, A., Gundersen, K., Alendal, G., Skaug, H., Gulliksson, M., Avlesen, H., Berntsen, J., Blackford, J., Cazenave, P., 2018. Simplified Modelling as a Tool to Locate and Quantify Fluxes from a CO2 Seep to Marine Waters, 14th Greenhouse Gas Control Technologies Conference Melbourne, pp. 21–26.

Omar, A.M., García-Ibáñez, M.I., Schaap, A., Oleynik, A., Esposito, M., Jeansson, E., Loucaides, S., Thomas, H., Alendal, G., 2021. Detection and quantification of CO2 seepage in seawater using the stoichiometric Cseep method: results from a recent subsea CO2 release experiment in the North Sea. Int. J. Greenhouse Gas Control 108, 103310.

Roche, B., Bull, J.M., Marin-Moreno, H., Leighton, T., Falcon-Suarez, I.H., White, P.R., Provenzano, G., Tholen, M., Lichtschlag, A., Li, J., Faggetter, M., 2021. Time-lapse imaging of CO2 migration within near-surface sediments during a controlled sub-seabed release experiment. Int. J. Greenhouse Gas Control 109.

Rodil, I.F., Attard, K.M., Norkko, J., Glud, R.N., Norkko, A., 2019. Towards a sampling design for characterizing habitat-specific benthic biodiversity related to oxygen flux dynamics using Aquatic Eddy Covariance. PLoS ONE 14, e0211673.

Romanak, K., Sherk, G.W., Hovorka, S., Yang, C., 2013. Assessment of alleged CO2 leakage at the Kerr farm using a simple process-based soil gas technique: implications for carbon capture, utilization, and storage (CCUS) monitoring. Energy Procedia 37, 4242–4248.

Rovelli, L., Dengler, M., Schmidt, M., Sommer, S., Linke, P., McGinnis, D.F., 2016. Thermocline mixing and vertical oxygen fluxes in the stratified central North Sea. Biogeosciences 13, 1609–1620.

Sawada, Y., Tanaka, J., Suzuki, C., Tanase, D., Tanaka, Y., 2018. Tomakomai CCS demonstration project of Japan, CO2 injection in progress. Energy Procedia 154, 3–8.

Schaap, A., Koopmans, D., Holtappels, M., Dewar, M., Arundell, M., Papadimitriou, S., Hanz, R., Monk, S., Mowlem, M., Loucaides, S., 2021. Quantification of a subsea CO2 release with lab-on-chip sensors measuring benthic gradients. Int. J. Greenhouse Gas Control 110, 103427.

Schumann, D., Duetschke, E., Pietzner, K., 2014. Public perception of CO2 offshore storage in Germany: regional differences and determinants. Energy Procedia 63, 7096–7112.

Sellami, N., Dewar, M., Stahl, H., Chen, B., 2015. Dynamics of rising CO2 bubble plumes in the QICS field experiment: part 1–The experiment. Int. J. Greenhouse Gas Control 38, 44–51.

Stull, R.B., 2012. An Introduction to Boundary Layer Meteorology. Springer Science & Business Media.

Vangkilde-Pedersen, T., Anthonsen, K.L., Smith, N., Kirk, K., van der Meer, B., Le Gallo, Y., Bossie-Codreanu, D., Wojcicki, A., Le Nindre, Y.-M., Hendriks, C., 2009. Assessing European capacity for geological storage of carbon dioxide–the EU GeoCapacity project. Energy Procedia 1, 2663–2670.

Vielstädte, L., Linke, P., Schmidt, M., Sommer, S., Haeckel, M., Braack, M., Wallmann, K., 2019. Footprint and detectability of a well leaking CO2 in the Central North Sea: implications from a field experiment and numerical modelling. Int. J. Greenhouse Gas Control 84, 190–203.

Wilczak, J.M., Oncley, S.P., Stage, S.A., 2001. Sonic anemometer tilt correction algorithms. Boundary Layer Meteorol. 99, 127–150.

Zeebe, R.E., Wolf-Gladrow, D., 2001. CO2 in seawater: equilibrium, kinetics, Isotopes. Gulf Professional Publishing.